Classification: Biological Sciences: Biophysics

Transient protonation changes in channelrhodopsin-2 and their relevance to channel gating

Víctor A. Lórenz-Fonfría[a], Tom Resler[a], Nils Krause[a], Melanie Nack[a], Michael Gossing[b], Gabriele Fischer von Mollard[b], Christian Bamann[c], Ernst Bamberg[c], Ramona Schlesinger[a], and Joachim Heberle[a,1]

[a] Freie Universität Berlin, Experimental Molecular Biophysics, Arnimallee 14, 14195 Berlin;
[b] Bielefeld University, Biochemistry (BC3), Universitätsstrasse 25, 33615 Bielefeld
[c] Max-Planck-Institute of Biophysics, Max-von-Laue-Straße 3, 60438 Frankfurt am Main, Germany.

[1] To whom correspondence should be addressed.
e-mail: joachim.heberle@fu-berlin.de

ABSTRACT

The discovery of the light-gated ion channel channelrhodopsin (ChR) set the stage for the novel field of optogenetics where cellular processes are controlled by light. Yet, the underlying molecular mechanism of light-induced cation permeation in ChR2 remains unknown. Here, we have traced the structural changes of ChR2 by time-resolved FT-IR spectroscopy, complemented by functional electrophysiological measurements. For the first time we have resolved the vibrational changes associated with the open states of the channel (P_2^{390} and P_3^{520}) and characterized several proton transfer events. Analysis of the amide I vibrations suggests a transient increase in hydration of transmembrane α-helices with $\tau_{1/2}$ = 60 μs which tally the onset of cation permeation. Aspartate 253 accepts the proton released by the Schiff base ($\tau_{1/2}$ = 10 μs), the latter being reprotonated by aspartic acid 156 ($\tau_{1/2}$ = 2 ms). The internal proton acceptor and donor groups, corresponding to D212 and D115 in bacteriorhodopsin, are clearly different to other microbial rhodopsins indicating that their spatial position in the protein was relocated during evolution. Previous conclusions on the involvement of glutamic acid 90 in channel opening are ruled out by demonstrating that E90 deprotonates exclusively in the non-conductive P_4^{480} state. Our results merge into a mechanistic proposal that relates the observed proton transfer reactions and the protein conformational changes to the gating of the cation channel.

Keywords

Bacteriorhodopsin – proton transfer – step-scan FT-IR – optogenetics – rhodopsin

SAMPLE SIGNIFICANCE STATEMENT

It always was a dream to control cells and living animals by light. The discovery of channelrhodopsin turned the dream into reality as this light-activated cation channel is able to elicit action potentials with unprecedented spatial and temporal resolution. To unravel the underlying molecular mechanism, we have applied time-resolved infrared spectroscopy and suggest how the observed proton transfer and the protein conformational changes lead to opening of the cation channel. Our results will not only contribute to the rational design of channelrhodopsin variants with improved properties but also help to develop general principles on the temporal sequence in the gating of ion channels.

INTRODUCTION

Optogenetics provides new tools to neurophysiologists to steer cellular responses with unprecedented temporal and spatial resolution. The former takes advantage of light as an ultrashort trigger while the latter is achieved by genetically encoding and directing photosensitive proteins to specific cell types. The most prominent among the optogenetics tools is channelrhodopsin (ChR) which was found to be the first light-gated ion channel of its kind (1, 2). This discovery paved the way for the exponentially growing number of neurophysiological applications ranging from single cells to living animals (3). Light-gated ion permeation by ChR expands the various modes of action of the large family of microbial rhodopsins already comprising light-driven ion pumps and sensors (4). Among the various ChRs which differ mostly in cation selectivity (3), ChR2 is employed in the majority of optogenetic applications because of the higher expression yield in mammalian cells.

A projection structure of the hepta-helical ChR2 showed a dimer with the contact interface between helices C and D, suggested to form the cation channel (5). More recently, a chimeric ChR (C1-C2) was constructed by linking the last two helices (F and G) of ChR2 to the first five (A to E) of ChR1 and resolved by X-ray crystallography to 2.3 Å (6). The high-resolution structure confirmed the dimeric arrangement and identified an electronegative extracellular pore in each monomer framed by helices A, B, C and G. Accompanying electrophysiological experiments on point mutants indicated residues in the glutamate-rich helix B that delineate the cation channel (6). It is surprising that mutations of either C128 or D156 in ChR2 lead to far more drastic functional alterations with intensified photocurrents and strongly retarded ground-state recovery kinetics (7) as these residues are located in helices C and D, respectively, i.e. remote from the proposed cation channel. The interaction of C128 and D156 was shown by FT-IR difference spectroscopy to involve an H-bond between the termini of both side chains, the so-called DC gate (8). The structural basis of the DC gate could not be corroborated by the crystallographic model of C1-C2, where the terminal S─H of C128 points away from D156 (6).

Like in all other microbial rhodopsins, ChR is energized by the photo-induced isomerization of retinal. This feature renders ChR unique among all ion channels as the functional mechanism can be studied over the time-scale from femtoseconds to seconds via triggering by a short light pulse. The chromophore retinal, linked to channelopsin via a protonated Schiff base (SB) with K257, exhibits an absorption maximum (λ_{max}) at ~470

nm in the dark state (9). The electronic properties of the retinal are modulated by the electrostatic structure in its immediate vicinity as ChR2 passes through a series of intermediate states (10). The photoreaction of ChR2 under continuous illumination is complex due to multiple photonic excitation (10) but single turnover conditions simplify the analysis when short laser pulses are applied (**Fig. 1**). Upon all-*trans* to 13-*cis* isomerization of the retinal cofactor and vibrational relaxation, the early red-shifted P_1^{500} intermediate ($\lambda_{max} \approx 500$ nm) is formed in the picosecond range (11). Subsequently, the retinal SB deprotonates and the blue-shifted P_2^{390} state ($\lambda_{max} \approx 390$ nm) is formed with $\tau_{1/2} \approx 10$ µs. Reprotonation of the SB proceeds with $\tau_{1/2} \approx 2$ ms, leading to the late red-shifted P_3^{520} state ($\lambda_{max} \approx 520$ nm), decaying with $\tau_{1/2} \approx 10$ ms to the late P_4^{480} state ($\lambda_{max} \approx 480$ nm). Relaxation of P_4^{480} to the original ground state is unusually slow for a retinylidene protein and proceeds with $\tau_{1/2} \approx 20$ s.

The groups accepting and donating the proton from and to the SB are yet unknown as well as the proton transfer reactions responsible for the observed proton pump activity of ChR2 (12). Correlation of time-resolved UV/Vis and electric experiments showed that the P_3^{520} state represents the conductive state (9). While closing the channel is clearly associated with P_3^{520} decay, opening appeared to occur before the rise of P_3^{520} but after the rise of the preceding P_2^{390} state (9, 10). FT-IR difference spectroscopy suggested large conformational changes in the protein backbone to take place in the early P_1^{500} and the late P_4^{480} states which were trapped under continuous illumination (13, 14). Structural information on the P_2^{390} and P_3^{520} states where opening and closing of the channel occurs is scarce, however.

Inasmuch the X-ray crystallographic structure sets the stage, the elucidation of the functional mechanism of ChR2 requires the contribution of time-resolved methodologies with appropriate structural sensitivity. IR difference spectroscopy is a powerful technique, being sensitive not only to the transient conformational changes of the protein but particularly to protonation and H-bonding changes of amino acid side chains. Here, we have used time-resolved step-scan FT-IR spectroscopy to study the photocycle of ChR2 with a time resolution of 6 µs, sufficient to probe the rise and decay of the conductive P_2^{390} and P_3^{520} intermediates and to trace the associated internal proton transfers. We conclude that the primary acceptor of the proton of the retinal SB is D253 (D212 in bacteriorhodopsin, bR) and the internal donor is D156 (D115 in bR), the latter accounting for the functional relevance of the DC gate. These results are drastically different to bR where D85 (E123 in ChR2) and D96 (H134 in ChR2) are the primary

proton acceptors and donors (15), and where D115 (D156 in ChR2) plays only an indirect role in the proton pump mechanism (16). Analysis of the time evolution of the conformationally sensitive amide I vibrations of the protein backbone suggests an increase in hydration of transmembrane α-helices which correlates to the onset of cation permeation. The hydration may be the result of the formation of a continuous water-filled channel inside the protein from previously disconnected internal cavities. We infer that the conformational rearrangements are triggered by changes in electrostatics and H-bonding networks that are a consequence of the observed protonation changes.

RESULTS

The conformational changes of ChR2 were studied by time-resolved FT-IR spectroscopy following photonic excitation by a pulsed laser emitting at 450 nm. The IR difference spectra displayed a rich and complex pattern of positive and negative peaks (**Fig. 2a**) reflecting a temporal sequence of conformational changes of the holoprotein as a consequence of the photo-induced isomerization of the chromophore retinal. The IR data were complemented by time-resolved UV/Vis experiments (**Fig. 2b**), used to define the time of maximum transient concentration of the respective photo-intermediates: 6 µs after the laser flash for the P_1^{500} state, 300 µs for the P_2^{390} state, 6 ms for the P_3^{520} state, and 300 ms for the P_4^{480} state (**Fig. 3**). This study is the first one to report on IR difference spectra of the conducting P_2^{390} and P_3^{520} states of ChR2, as well as for the early P_1^{500} state recorded at room temperature.

The negative bands in **Fig. 3a** represent vibrations of the dark state of ChR2 which are missing in the respective intermediate states. The appearance of negative bands at 1240, 1200 and 1154 cm^{-1}, typical for C─C stretching vibrations of all-*trans* retinal (17), are in accordance with the general view that the photocycle of ChR2 originates mostly from the photo-isomerization of all-*trans* retinal (10). The negative band at 1554 cm^{-1} is due to the ethylenic (C═C) vibration of ground-state retinal (18). The frequency correlates well with the electronic absorption of retinal at 470 nm of ground-state ChR2 (19).

The time-resolved IR difference spectrum of the P_1^{500} state (top spectrum in **Fig. 3a**) exhibits similar spectral changes in the amide I region (negative band at 1663 cm^{-1}) as the state trapped at 80 K (13, 14), albeit with discrepancies at other frequencies (**Fig. S1a**). Thus, the large amide I changes previously found in static difference spectra, were not due to a cryogenic artifact but are related to unusually fast conformational changes of the protein backbone. The time-resolved difference spectrum of the P_1^{500} intermediate shows a positive band at 986 cm^{-1} assigned to hydrogen-out-of-phase (HOOP) vibrations of the retinal, indicating a non-planar retinal conformation in the early red-shifted intermediate as in other microbial rhodopsins (20-22). The positive band at 1173 cm^{-1} appears asymmetric and strongly red-shifted with respect to the C_{14}─C_{15} stretching of 13-*cis* retinal in other microbial rhodopsins (1190-1187 cm^{-1} (20-22)). Its asymmetric shape with a shoulder at 1188 cm^{-1} (**Fig. 3a** and **Fig. S2**) reflects heterogeneity in the conformation of the isomerized retinal suggesting contributions from an intermediate preceding P_1^{500}. Two positive bands assignable to the retinal C_{14}─C_{15} stretching vibration

were also observed in proteorhodopsin (23), with a dark state composed of a 70:30 mixture of all-*trans* and 13-*cis* retinal like in ChR2 (18). Thus, it is inferred that the spectral heterogeneity of the C_{14}─C_{15} stretching might as well indicate the concurrence of photo-intermediates from both the all-*trans* and the 13-*cis* retinal photocycles, as was found in *Anabaena* sensory rhodopsin (24).

At 300 µs after the laser pulse, the P_2^{390} state is the predominant intermediate as indicated by positive absorption at 375 nm in the UV/Vis difference spectrum (**Fig. 3b**). However, residual absorption at around 520 nm is also observed. Thus, the IR difference spectrum recorded at 300 µs includes minor contributions from a red-shifted intermediate state (**Fig. 3a**). A pure difference spectrum of the subsequent P_3^{520} intermediate was isolated at 6 ms after the laser flash (**Fig. 3b**). The positive band at 1542 cm^{-1} is assigned to the ethylenic vibration of retinal (**Fig. 3a**). The frequency correlated well with the absorption maximum at 520 nm (19). The positive band from the C_{14}─C_{15} stretching of the isomerized retinal shifted to 1177 cm^{-1} in P_3^{520} which reflects different retinal conformations in the P_1^{500} and P_3^{520} intermediate states. The difference spectrum of the P_4^{480} state was resolved at 300 ms after the laser pulse. The absorption band of the ethylenic vibration of ground-state retinal is largely canceled due to the similar frequency of this mode in the P_4^{480} state (**Fig. 3a**). The IR difference spectrum of P_4^{480} is largely identical to the spectrum obtained under continuous illumination (**Fig. S1b**) and very similar to the time-resolved difference spectrum of P_4^{480} when ChR2 is reconstituted in liposomes (25).

Proton transfer and hydrogen-bonding changes involving aspartate and glutamate side chains. The retinal Schiff base of ChR2 deprotonates in the P_1^{500}-to-P_2^{390} and is reprotonated in the P_2^{390}-to-P_3^{520} transition (9). The groups accepting and donating the proton from and to the SB are yet unknown but prime candidates are the terminal carboxylic groups of aspartate or glutamate residues and their corresponding acids as in other well-characterized rhodopsins. IR difference spectroscopy is particularly suited for the identification of protonation changes (26-28) because the C═O stretching vibration (νC═O) of protonated carboxylic groups appear in the 1780-1690 cm^{-1} frequency range (29, 30). The vibrational bands in the carboxylic region of the four intermediate states exhibit significant spectral overlap (**Fig. 3a** and **Fig. S2**) which is reduced by applying a well-established band-narrowing method (Fourier self-deconvolution, FSD) (31) to the IR difference spectra (**Fig. 4a**). By these means, up to four positive (1760, 1745, 1728, and

1695 cm^{-1}) and two negative (1737 and 1717 cm^{-1}) bands were resolved (**Fig. 4a**). The assignment of these vibrational bands to molecular changes and the implications on the molecular mechanism of ChR2 will be discussed in the following.

Primary proton donor to the retinal Schiff base. The rationale for the identification of the internal proton donor is that deprotonation of an aspartic or glutamic acid will generate a negative band whose kinetics match those of the formation of the P_3^{520} state. Two negative bands were resolved in the carboxylic region (**Fig. 4a**) but only the kinetics of the band at 1737 cm^{-1}, matched the rise and decay of the P_3^{520} state (**Fig. 4b**). In the IR difference spectrum of the P_3^{520} intermediate of D156E the negative peak at 1737 cm^{-1} is up-shifted to 1763 cm^{-1} while the negative band at 1717 cm^{-1} is not affected (**Fig. 4d**, frequency-shift indicated by an arrow). We generated the wild-type minus D156E double difference spectrum firmly establishing that the negative peak at 1737 cm^{-1} in P_3^{520} originates from deprotonation of D156 and not from an environmental change (**Fig. S5a**). As expected, the negative band at 1737 cm^{-1} vanished in the IR difference spectrum of the P_2^{390} intermediate of the D156A variant as also did the bands at 1760 and 1745 cm^{-1} (**Fig. 4d**, bands marked by asterisks). Thus, these two positive bands reflect H-bonding changes of the D156 carboxylic group in the P_1^{500} and P_2^{390} states, respectively. The remaining bands at 1717 and 1728 cm^{-1} disappeared in the E90A variant (**Fig. S4**), which supports their assignment to the $\nu C{=}O$ of the terminal carboxylic acid of E90 in the dark and photolyzed states, respectively (14).

As D156 was identified as the internal proton donor to the retinal Schiff base, we addressed the consequences of replacement of this residue by recording photocycle kinetics and channel functionality of D156 variants. The kinetics of SB reprotonation was accelerated in the D156E variant leading to low P_2^{390} accumulation (**Fig. 5a**). The subsequent reprotonation of E156 was slowed down resulting in a 10-fold delayed P_3^{520} decay (**Fig 5b**). Both effects suggest a reduced proton affinity of the proton donor as a result of the D156E replacement. The D156E variant retains activity as demonstrated by electrophysiology (**Fig. 6 and S3b,c**). In agreement with the slower P_3^{520} decay, closing of the channel was also 10-fold delayed with respect to the wild type (**Fig. 6**). It was previously shown that although the D156A variant is functional in cation permeation, it exhibits a ~10^4-fold delayed reprotonation of the retinal Schiff base and strongly retarded channel closure (7), an observation that can now be rationalized by the absence of a

suitable internal proton donor. In conclusion, we infer that the reprotonation of D156 is a molecular determinant for efficient channel closure.

Primary acceptor of the Schiff base proton. The crystallographic structure of the C1-C2 chimera (6) locates E123 and D253 3.4 Å and 3.0 Å away from the retinal Schiff base (shortest distance). The close proximity renders these residues prime candidates as acceptors of the Schiff base proton. However, a positive band for the νC=O frequency of the SB proton acceptor, clearly observed in other rhodopsins in the range of 1765-1710 cm^{-1} (**Table S1**), is evidently missing in the P_2^{390} state IR difference spectrum of wild-type ChR2 (**Fig. 3a**). The three observed positive bands above 1710 cm^{-1} can be exclusively assigned to H-bonding changes of D156 and E90. As the latter two residues are both protonated in the dark state of ChR2, they cannot serve as proton acceptors of the SB proton after light excitation.

The only positive band left in the difference spectrum of P_2^{390} (**Fig. 4a**) is the band at 1695 cm^{-1}. The rise kinetics of this band tallies the rise of the P_2^{390} state (**Fig. 7b**), i.e., compatible with the expected kinetics of the SB proton acceptor. However, the frequency is unusually low for a carboxylic νC=O (32) and changes in the C=O stretching vibration of glutamine and asparagine side chains and of peptide bond vibrations may appear as well in this frequency range (32). Thus, we recorded time-resolved FT-IR difference spectra of E123 and D253 variants to identify the internal proton acceptor group.

The equivalent residue to E123 of ChR2 is D85 of bR which was shown to be the primary proton acceptor of the Schiff base. Therefore, we replaced E123 by T and expected similar strong impact on the functionality as the equivalent D85T mutation in bR (33). However, the replacement barely affected P_2^{390} and P_3^{520} formation and decay kinetics (**Fig. 5**) which agrees well with the preserved channel activity of the E123T variant as was reported by Gunaydin *et al.* (34). Consistent with these observations, the IR difference spectrum of the P_2^{390} state of ChR2 is only moderately affected by the E123T mutation (**Fig. S4**). A distinct difference, however, is the appearance of the positive band at 1712 cm^{-1} (**Fig. 7a**). The kinetics of the rise of this band tallied the rise of the P_2^{390} intermediate (**Fig. 7c**). The double difference spectrum between wild type and the E123T variant (**Fig. S5b**) shows difference bands at 1715(–)/1697(+) cm^{-1}. The positive band at 1715 cm^{-1} is assigned to the νC=O stretch of D253 (*vide infra*) which is up-shifted in the E123T variant. The positive band is apparently preserved in the succeeding P_3^{520} state of the E123T mutant, albeit slightly down-shifted to 1708 cm^{-1} by

a change in hydrogen bonding (**Fig. S4**). Thus, the proton acceptor remains protonated in P_3^{520}.

The results of the E123T variant with its modestly affected kinetics and spectra, point to D253 as the Schiff base proton acceptor. We scrutinized this possibility by studying the functionally active D253E variant (**Fig. 6** and **S3a,c**), which exhibited a notable 50-fold acceleration of the rise of the P_2^{390} state **(Fig. 5a)**. The decay of the P_2^{390} state was 3-times slower upon D253E replacement, leading to a low and delayed P_3^{520} accumulation **(Fig. 5b)** and, correspondingly, to retarded channel closure (**Fig. 6**). Despite the conservative exchange of D vs. E, the D253E mutation led to alterations in the IR difference spectrum of the P_2^{390} state exceeding by far those of E123T (**Fig. S4**). A new positive band at 1709 cm^{-1} (**Fig. 7a**) is observed in the IR difference spectrum of D253E in the P_2^{390} state whose kinetics matches the rise of the P_2^{390} state (**Fig. 7d**). In analogy to the E123T replacement, the newly appearing positive band in the D253E variant is accompanied by a decrease of the area of the band at 1695 cm^{-1} (**Fig. 7a**). The pair of bands in the double difference spectrum between wild-type and D253E, at 1712(–)/1696(+) cm^{-1} (**Fig. S5c**), is consistent with the νC═O frequency of protonated E253 and D253, respectively. The IR difference spectrum of the D253N variant showed significant alterations (**Fig. S4**), most notably in the carboxylic region. Firstly, the 1717/1728 cm^{-1} band feature vanished completely (**Fig. 7a**) suggesting that the D253N replacement destabilized also the protonated form of E90 in dark-state ChR2. Secondly, a positive band from the proton acceptor did not appear above 1700 cm^{-1}, unlike in the functionally active E123T and D253E variants (**Fig. 7a**). The D253N mutation did not exhibit channel behavior (**Fig. S3c**) even though the amino acid exchange hardly affected the kinetics of the P_2^{390} and P_3^{520} states (**Fig. S7**).

Protonation changes of E90. The negative band at 1717 cm^{-1} in the difference spectrum of P_4^{480} (**Fig. 4a**) has previously been assigned to the νC═O of E90 (25). However, the latter work could not to resolve the onset of deprotonation of E90 due to insufficient time resolution. The blue trace in **Fig. 4c** shows that the negative band at 1717 cm^{-1} reached maximal intensity before 6 µs and decayed in two well-separated phases. The first phase mirrors the kinetics of the positive band at 1728 cm^{-1} (**Fig. 4c**, green trace) suggesting a shift in the νC═O vibration of protonated E90 from 1717 cm^{-1} to 1728 cm^{-1} early in the photocycle. The deprotonation kinetics have been separated from H-bonding changes of E90 by adding the kinetic traces at 1728 cm^{-1} and at 1717

cm^{-1} (**Fig. 4c**, magenta trace), clearly revealing that the deprotonated state of E90 is present only during the lifetime of the P_4^{480} intermediate.

Structural changes of the protein backbone. Conformational and environmental changes in the protein backbone are reflected in frequency changes of the amide I vibrations comprising predominantly the νC═O mode of the peptide backbone (35). Steady-state IR difference spectra recorded under continuous illumination have shown intense bands in the range of α-helices, namely a negative peak at 1663 cm^{-1} and a positive peak at 1648 cm^{-1} (13, 14). Interestingly, the intense negative difference band appeared also when illuminating ChR2 at 80 K, arguing for large structural changes even at cryogenic temperatures. Our time-resolved data confirms the presence of the negative band at 1663 cm^{-1} that persisted from 6 µs until the end of the photocycle albeit with varying intensity (**Fig. 8a)**. The intense positive band at 1650 cm^{-1} is weak at 6 µs but rises in intensity later on. Despite their different initial intensity, the transient intensity changes of the bands at 1663 (–) and 1650 cm^{-1} (+) followed a similar temporal profile suggesting a frequency downshift of the amide I band (**Fig. 8b)**. The time traces of both bands reached maxima at 1 ms, i.e. in between the maximal concentrations of the P_2^{390} (350 µs) and P_3^{520} (4 ms) states. The maximal photocurrent amplitude in ChR2 is also detected at 1 ms after photo-excitation (**Fig. 6** and (9)). However, the rise of the changes at 1650 cm^{-1} (**Fig. 8b**, green trace) lags behind the deprotonation of the SB (**Fig. 8b**, gray trace), with $\tau_{1/2}$ of 60 µs vs. 10 µs, respectively. This delay suggests the presence of two P_2^{390} substates with the transition between them linked to the onset of protein backbone alterations.

Structural changes are also reflected in the amide II vibration of the protein backbone, a coupled mode of the C─N stretching and N─H in-plane bending vibrations (35). **Figure 8e** shows the IR difference spectrum at 300 ms after the laser pulse, i.e. when P_4^{480} dominates. This time was chosen because here the ethylenic vibrations of the retinal, overlapping in frequency with the amide II, are reduced in intensity in P_4^{480}. Indeed, bands are observed at 1561(+)/1541(–) cm^{-1}, in the range of α-helical structures (35). It was deduced from experiments and simulations that the hydration of α-helices shifts the amide I vibration frequency down by 8-20 cm^{-1} due to H-bonding of water to the amide C═O (36, 37). Correspondingly, a frequency up-shift is expected for the amide II frequency, given that the H-bonding of water to the amide C═O will weaken the H-bond between amide C═O and N─H pairs, leading to a stronger N─H bond. Thus, the bands

at 1663(–)/1650(+) cm^{-1} and at 1561(+)/1540(–) cm^{-1} may report the hydration of α-helices during the ChR2 photocycle, i.e. transient access of bulk water to parts of the transmembrane region.

The appearance of the two intense bands at 1663(–)/1631(+) cm^{-1} as soon as 6 µs after pulsed laser excitation (**Fig. 8a**) indicates that some protein backbone changes precede the hydration of helices. The two bands exhibit the same kinetics after accounting for overlapping contributions (**Fig. 8c**). Based on their frequencies they can be tentatively assigned to the sub-microsecond elongation of β-hairpins (1640-1625 cm^{-1} (35)) from extra-membrane loops (~1662 cm^{-1} (38)). However, the negative absorption at 1663 cm^{-1} may also comprise changes in the νC=N of the protonated SB, the frequency of which has been assigned to 1657 cm^{-1} by resonance Raman spectroscopy (18).

There is consensus that the channel of ChR2 closes with P_3^{520} decay ($\tau_{1/2} \approx 10$ ms) (9, 10). We probed the recovery of the initial dark state by recording the integrated area of the retinal band at 1240 cm^{-1} (mostly C_{12}–C_{13} stretching of ground-state all-*trans* retinal (17)), as done before for bR (39). The kinetics are clearly bi-phasic where the dominant phase (75%) proceeded concomitant to P_3^{520} decay, with $\tau_{1/2} \approx 10$ ms **(Fig. 8d)**. The remaining 25% of the molecules decay ~1.000 times slower ($\tau_{1/2} \approx 20$ s), concomitant to P_4^{480} decay **(Fig. 8d).** This result indicates that the majority of ChR2 molecules decay directly to the initial dark state without passing the P_4^{480} state, presumably by a branch at the level of the P_3^{520} state. These molecules close the channel in the P_3^{520}-to-ChR2 transition by restoring the initial retinal and protein conformation. The fraction of ChR2 molecules that transit the P_4^{480} state close the channel without reverting most of the conformational changes in the protein backbone, as indicated by the very similar IR differences in the amide I region of the P_3^{520} and P_4^{480} states (**Fig. 8a**). Notably, the bands assigned to the hydration of transmembrane helices are quantitatively preserved in P_4^{480}, with the 1663/1650 cm^{-1} bands showing 25% of their maximal intensity at 300 ms (**Fig. 8b**).

DISCUSSION

We have traced the molecular changes of photo-activated ChR2 by time-resolved IR difference spectroscopy. By spectral and kinetic analysis, the timing of the protonation and deprotonation of three crucial internal carboxylic groups was determined during opening and closing of the channel. The vibrational assignment was achieved with the help of the mutants E90A, E123T, D156E, D156A, D253E and D253N. We found that the terminal carboxylate of D253 gets protonated with the rise of the P_2^{390} intermediate (**Fig. 7**), i.e. when the retinal SB deprotonates. D156 deprotonates in the P_2^{390}-to-P_3^{520} transition, concomitantly to SB reprotonation (**Fig. 4a,b,d**). Thus, we assign D253 and D156 to act as internal proton acceptor and donor of the retinal SB, respectively. Finally, E90 deprotonates only in the P_4^{480} intermediate (**Fig. 4a,c**).

An acidic residue at position 253 but not at position 123 is conserved in all ChRs sequenced so far (40). While the replacement of D253 by non-protonatable residues lead to the loss of channel function (D253A in C1-C2 (6) and D253N in ChR2, see **Fig. S3**), the functionality of E123 variants is preserved even upon mutation to a non-polar residue like alanine (34). The role of D253 as the primary proton acceptor is further corroborated by the 50-fold accelerated deprotonation kinetics of the retinal SB in D253E (**Fig. 5**). The longer side chain of the glutamate residue might place the accepting carboxylate group closer to the positively charged SB leading to accelerate proton transfer by electrostatic coupling (41). Such behavior is reminiscent of the D85E mutant in bR (42).

The frequency of the νC═O vibration of protonated D253 is 1696 cm^{-1}, low enough to challenge its identification. For such low vibrational energy to occur, the C═O group must interact with an H-bonding donor and the O─H group must be H-bonded to a strong acceptor (29, 30). νC═O frequencies lower than 1700 cm^{-1} have been reported for carboxylic groups only when the H-bonding donor is the NH_3^+ group from a lysine (29, 30) or when the H-bond acceptor is a COO^- group (43). Thus, we infer that the terminal carboxylate of E123 is the H-bond acceptor of protonated D253 in the P_2^{390} state of ChR2 (**Fig. 9a**). The strong interaction of the carboxylic O─H group of D253 with the E123 carboxylate is weakened by the E123T replacement which leads to the observed frequency up-shift of the νC═O of protonated D253 from 1696 cm^{-1} to 1715 cm^{-1} (**Fig. 7, S5b**). A similar frequency up-shift occurs in D253E (**Fig. 7, S5c**) where the

aforementioned H-bond with E123 would be geometrically less favorable by the longer side chain of E253.

The identification of D156 as internal proton donor to the SB explains the extremely long lifetime of the P_2^{390} intermediate in the D156A variant (7). In the absence of the internal proton donor, SB reprotonation is rate-limiting for the photocycle. We may infer a strongly pH-dependent photocycle kinetics in D156A, akin the D96 variants of bR (44). Moreover, we are now in a position to rationalize the kinetic alterations found in variants of C128 (7), a residue H-bonded to D156 to form the DC gate (8). One of the roles of the DC gate could be to raise the pK_a of D156. Upon C128A and C128T mutations, the deprotonated state of D156 is stabilized which provides a clue to the long lifetime of the P_3^{520} state in these mutants (7). We suggest that the pK_a of D156 is lowered in C128 variants, to be even deprotonated in ground-state ChR2 at neutral pH, as was observed for D115 in bR by the homologous T90A mutation (45). A partially deprotonated D156 in the dark state and, thus, a pH-dependent inactive fraction of the primary proton donor, elegantly explains why a long-lived P_2^{390} state is present in C128 mutants and why the P_2^{390} accumulates with increasing pH (7).

The observed proton transfer reactions are put into structural context (**Fig. 9b**) using the structural model of ChR2 based on the recent X-ray crystallographic data of the C1-C2 chimera (6). In this scheme, D253 accepts the proton from the SB with a half-life of ~10 μs. The SB is reprotonated from D156 with a half-life of ~ 2 ms. The latter two groups are 9.7 Å apart which is comparable to the 12.0 Å distance between the SB and D96 in bR (46). We recently monitored transient pH changes in the aqueous medium with the help of a pH-indicating dye (47). Proton release to the bulk aqueous medium was detected with the rise of the P_3^{520} state. Since D253 appears to remain protonated in P_3^{520}, we postulate the presence of a proton release group (PRG) in ChR2.

The recovery kinetics of the initial dark state proceeds in two well-separated phases (**Fig. 8d**) which is explained by branching out of the ChR2 photocycle at the level of the P_3^{520} intermediate. About 75% of the ChR2 molecules relax from P_3^{520} directly to the ground state, taking up a proton from the bulk to reprotonate D156. In the remaining 25% of the population, E90 releases its proton and P_3^{520} relaxes to P_4^{480}. Finally, protons will be taken up from the cytoplasm to reprotonate E90 in the P_4^{480}-to-ChR2 transition. The latter interpretation is corroborated by pH indicator experiments on the E90A variant where the slow phase of proton uptake was absent (**Fig. S8**). In the pH indicator

experiments on wild-type ChR2, the slow phase exhibits a relative amplitude of 20% (47) which is close to the 25% fraction derived to transit the P_4^{480} state.

Large changes in amide I bands have been observed during the course of the photocycle which were previously suggested to reflect conformational changes in the backbone of the transmembrane α-helices (13, 14). Moreover, we found opposite frequency shifts for the amide I and amide II vibrations which were interpreted to arise from the transient hydration of some transmembrane α-helices. The putative backbone hydration takes place after SB deprotonation, at a time that coincides with the onset of channeling activity as reported by time-resolved electrical measurements (9). P_3^{520} is generally accepted to be the conductive state of ChR2 (10), and so the structural changes reporting the hydration of transmembrane helices appear to take place too early to be related to the opening of the channel. However, compelling evidence for P_2^{390} being also conductive comes from the D156A variant. Although it shows a long-lived P_2^{390} intermediate and barely any P_3^{520} formation, the ion conductance is as high as in C128 mutants that exhibit long-lived P_3^{520} states (7). Thus, we may infer on the existence of two consecutive P_2^{390} states with different peptide backbone structures that relate to the opening of the ion gate.

From the X-ray structural model, a pore was suggested to intrude from the extracellular medium which is framed by transmembrane helices A, B, C and G (6). E90 (on helix B), H-bonded to N258 (on helix G), is located at the tip of the intruding pore funnel (6). After light excitation, isomerization of all-*trans* retinal leads to the weakening of the H-bond between E90-N258, explaining the 11 cm^{-1} upshift of the νC=O vibration frequency in the early P_1^{500} state of the of E90 mutant (**Fig. 5a**, **c**). The structural consequences of retinal isomerization might reach the extramembrane loops on a sub-microsecond scale, leading to the elongation of β-hairpins (**Fig. 8c**), which are present in both the intra and extracellular domain of the C1-C2 crystallographic structure (6). The subsequent transfer of the proton from the SB to D253 may lead to tilting of some of the transmembrane helices surrounding the pore as in models proposed for voltage-gated ion channels (48). Mechanistically, this structural change will be driven by the re-organization of intramolecular H-bonding networks which follow retinal conformation and proton transfer from the SB to D253. Particularly, changes in H-bonds involved in inter-helical interactions, like e.g. those of the DC gate, might be critical to transduce electrostatic changes into pK_a and conformational changes (16). Indeed, the frequency change of the νC=O of D156 attests for the adaptive response of the DC gate during the

different steps of the photocycle (**Fig. 4a**). The tilt of helices will be sufficient to extend the length of the pore to the cytoplasmic medium, and will also lead to the hydration of transmembrane helices. Once formed, the conductivity and selectivity of the channel will be mostly regulated by residues facing the channel interior.

What remains elusive is the role of the deprotonation of E90 which takes place during the rise of the P_4^{480} state. Closure of the channel during the P_3^{520}-to-P_4^{480} transition does not require the reversal of the large protein structural changes (**Fig. 8a**). We infer that deprotonation of E90 leads to a transiently stronger H-bonding N258. The stabilized interaction may act as lock which constrains the dynamics of the adjacent helices that frame the channel, and by this way help to reduce the ion conductance. Saving the obvious differences, this scenario is reminiscent of the ionic lock between E134, R135 and E247 in bovine visual rhodopsin (49). E134 is ionic in the ground state and its transient protonation leads to the disruption of the salt bridge, identified as a thermodynamic contributor to the formation of the active state of rhodopsin. Similarly, deprotonation of E90 could contribute to the inhibition of the channel conductance upon continued illumination (desensitization) which was observed to be reduced (50) or even abolished (25) in E90 variants.

In conclusion, we have traced the sequence of proton transfer reactions in ChR2 by time-resolved IR spectroscopy. D253 was identified as the primary proton acceptor of the retinal Schiff base and D156 as the internal proton donor. Intriguingly, the proton donor and acceptor groups to the retinal Schiff base of ChR2 are different in location to all other microbial rhodopsins known so far.

The observed elementary reactions were related to molecular changes that eventually lead to on- and off-gating of the cation channel. Although neither D253 nor D156 are part of the putative ion channel, mutation of either of these two residues led to the most drastic alterations in the photocycle and channel behavior of ChR2 so far described. Namely, mutation of D253 to a non-protonable group prevents channel opening, while mutations of D156 strongly delay channel closure. Thus, the proton transfer reactions identified in the present work, are clearly rate-limiting to channel gating. But while the change in electrostatic pattern created by internal proton relocation appears intimately connected to channel gating the mechanistic link between both events remains still elusive. Yet, ChR2 is a unique ion channel as details of channel gating can be studied at high time resolution by the option of triggering and synchronizing channel activity by a

short laser pulse. Thus, it is possible to experimentally access intermediate states of ion permeation across the membrane in great detail which are usually hidden.

MATERIALS AND METHODS

Wild-type ChR2 and the point mutants E90A, E123T, D156E, D156A, D253E and D253N were heterologously expressed in *Pichia pastoris*. The His-tagged proteins were solubilized in 0.2% decyl maltoside (DM), 100 mM NaCl, 20 mM HEPES (pH 7.4) as described (8, 13). The resulting protein-detergent micelle sufficiently mimics the properties of the lipid bilayer as was concluded in previous spectroscopic studies (18, 51). For experiments measuring the transient pH changes of E90A, the buffer was substituted by 15 μM of the pH indicator bromoxylenol blue (47). Samples used for FT-IR spectroscopy were concentrated to ~ 4 mg/ml ChR2 in an aqueous solution of 5 mM NaCl and 5 mM HEPES at pH 7.4, and approximately 8 μl was dried on top of a BaF_2 window. The protein film was rehydrated with the saturated vapor phase of a glycerol/water mixture (3/7 w/w) (52). Sample hydration was sufficient as deduced from the absorbance IR spectrum (**Fig. S9**) and from the similar kinetics when compared with UV/Vis experiments performed on ChR2 in solution (**Table S2**). The hydrated films of ChR2 were placed into the FT-IR spectrometer (Vertex 80v, Bruker, Rheinstetten, Germany). Sample holder was kept at constant temperature by a circulating water bath set to 25^{o}C (Julabo F25). Time-resolved UV/Vis experiments were performed on these samples at specific wavelengths and on solubilized ChR2 in solution from 320 to 600 nm in 20 nm steps, using a commercial flash photolysis spectrometer (LKS80 from Applied Photophysics). The photoreaction in the IR and the UV/Vis experiments was induced by a short laser pulse emitted by a Nd:YAG laser (Quanta-Ray from Spectra-Physics) which drives an OPO (optical parametric oscillator from OPTA, Germany). The resulting emission was set to a wavelength of 450 nm with 10 ns pulse width and 3 mJ/cm^2 energy density at the sample, leading to a photo-conversion of about 10% of the molecules (47). Time-resolved step-scan FT-IR difference spectra were recorded in the time range of 6.25 μs to 125 ms. Rapid-scan FT-IR spectroscopy was used to trace the slower kinetic range (90 ms - 95 s). All data were recorded at a spectral resolution of 8 cm^{-1}. The repetition rate of the pulsed laser was set to 0.25 Hz for the step-scan and 0.01 Hz for the rapid-scan experiments, the former sufficiently fast to perform the experiments within reasonable time frame (5 days of data accumulation for wild-type ChR2) but slow enough to prevent artifacts from excitation of slow photocycle intermediates (**Fig. S11**). After data acquisition the time-resolved IR spectra were quasi-logarithmically averaged to 20 spectra per decade, and offset to zero in the range of

1820-1780 cm^{-1}. The step-scan and the rapid-scan data were merged and noise-filtered by singular value decomposition (SVD), retaining the first five major components (**Fig. S12**). Fourier self-deconvolution (FSD) and global fitting were applied as described in the **SI Materials and Methods**. The flash photolysis experiments in the UV/Vis range were performed on two times scales, the faster time range (<300 μs) recorded with the light source (Xe arc lamp) in pulsed mode and the slower time scale (>30 μs) with the lamp in continuous operation. Repetition frequency of the photolysis laser was 0.01 Hz. The kinetic data were quasi-logarithmic averaged (100 points/decade), and noise-reduced by SVD by retaining the first five major components. Difference spectra were generated by spline interpolation between the measured absorption changes at each wavelength (refer to **SI Materials and Methods** for a detailed description of the acquisition, processing and analysis of the time-resolved FT-IR data and of the electrophysiological recordings.

Acknowledgments

We thank D. Heinrich and I. Wallat for excellent sample preparation and technical support and T. Sattig (MPI) for help with the oocyte measurements. This work was supported by grants from the Deutsche Forschungsgemeinschaft to E.B. (SFB-807) and to J.H. (FOR-1279, SFB-1078), and from the Cluster of Excellence (Macromolecular Complexes) to E.B.

Author contributions

V.A.L.-F. performed FT-IR measurements, analyzed the spectroscopic data and wrote the paper. T.R. performed laser flash photolysis and FT-IR measurements. N.K. and R.S. purified wild-type ChR2, constructed and purified D253E and D253N mutants. M.N. purified the D156E mutant and performed initial flash-photolysis experiments. M.G. and G.F.M constructed and expressed the D156E mutant. C.B. and E.B performed and analyzed electrophysiological measurements and provided the E90A, E123T and D156A mutants. J.H. conceived the study, and wrote the paper. All authors discussed the results.

References

1. Nagel G*, et al.* (2003) Channelrhodopsin-2, a directly light-gated cation-selective membrane channel. *Proc. Natl. Acad. Sci U. S. A.* 100(24):13940-13945.

2. Nagel G*, et al.* (2002) Channelrhodopsin-1: a light-gated proton channel in green algae. *Science* 296(5577):2395-2398.

3. Zhang F*, et al.* (2011) The microbial opsin family of optogenetic tools. *Cell* 147(7):1446-1457.

4. Spudich JL (2006) The multitalented microbial sensory rhodopsins. *Trends Microbiol.* 14(11):480-487.

5. Muller M, Bamann C, Bamberg E, & Kuhlbrandt W (2011) Projection structure of channelrhodopsin-2 at 6 Å resolution by electron crystallography. *J. Mol. Biol.* 414(1):86-95.

6. Kato HE*, et al.* (2012) Crystal structure of the channelrhodopsin light-gated cation channel. *Nature* 482(7385):369-374.

7. Bamann C, Gueta R, Kleinlogel S, Nagel G, & Bamberg E (2010) Structural guidance of the photocycle of channelrhodopsin-2 by an interhelical hydrogen bond. *Biochemistry* 49(2):267-278.

8. Nack M*, et al.* (2010) The DC gate in Channelrhodopsin-2: crucial hydrogen bonding interaction between C128 and D156. *Photochem Photobiol Sci* 9(2):194-198.

9. Bamann C, Kirsch T, Nagel G, & Bamberg E (2008) Spectral characteristics of the photocycle of channelrhodopsin-2 and its implication for channel function. *J Mol Biol* 375(3):686-694.

10. Stehfest K & Hegemann P (2010) Evolution of the channelrhodopsin photocycle model. *ChemPhysChem* 11(6):1120-1126.

11. Verhoefen MK*, et al.* (2010) The photocycle of channelrhodopsin-2: ultrafast reaction dynamics and subsequent reaction steps. *Chemphyschem* 11(14):3113-3122.

12. Feldbauer K*, et al.* (2009) Channelrhodopsin-2 is a leaky proton pump. *Proc. Natl. Acad. Sci. U. S. A.* 106(30):12317-12322.

13. Radu I*, et al.* (2009) Conformational changes of channelrhodopsin-2. *J. Am. Chem. Soc.* 131(21):7313-7319.

14. Ritter E, Stehfest K, Berndt A, Hegemann P, & Bartl FJ (2008) Monitoring light-induced structural changes of Channelrhodopsin-2 by UV-visible and Fourier transform infrared spectroscopy. *J. Biol. Chem.* 283(50):35033-35041.

15. Heberle J (2000) Proton transfer reactions across bacteriorhodopsin and along the membrane. *Biochim. Biophys. Acta* 1458(1):135-147.

16. Perálvarez-Marín A*, et al.* (2007) Inter-helical hydrogen bonds are essential elements for intra-protein signal transduction: the role of Asp115 in bacteriorhodopsin transport function. *J. Mol. Biol.* 368:666-676.

17. Smith SO, Lugtenburg J, & Mathies RA (1985) Determination of retinal chromophore structure in bacteriorhodopsin with resonance Raman spectroscopy. *J Membr Biol* 85(2):95-109.

18. Nack M, Radu I, Bamann C, Bamberg E, & Heberle J (2009) The retinal structure of channelrhodopsin-2 assessed by resonance Raman spectroscopy. *FEBS Lett.* 583(22):3676-3680.

19. Aton B, Doukas AG, Callender RH, Becher B, & Ebrey TG (1977) Resonance Raman studies of the purple membrane. *Biochemistry* 16(13):2995-2999.

20. Dioumaev AK & Braiman MS (1997) Two bathointermediates of the bacteriorhodopsin photocycle, distringuished by nanosecond time-resolved FTIR spectroscopy at room temperature. *J. Phys. Chem. B* 101:1655-1662.

21. Hackmann C*, et al.* (2001) Static and time-resolved step-scan Fourier transform infrared investigations of the photoreaction of halorhodopsin from *Natronobacterium pharaonis*: consequences for models of the anion translocation mechanism. *Biophys. J.* 81(1):394-406.

22. Hein M, Wegener AA, Engelhard M, & Siebert F (2003) Time-resolved FTIR studies of sensory rhodopsin II (NpSRII) from *Natronobacterium pharaonis*: implications for proton transport and receptor activation. *Biophys J* 84(2 Pt 1):1208-1217.

23. Friedrich T*, et al.* (2002) Proteorhodopsin is a light-driven proton pump with variable vectoriality. *J. Mol. Biol.* 321(5):821-838.

24. Kawanabe A, Furutani Y, Jung KH, & Kandori H (2006) FTIR study of the photoisomerization processes in the 13-*cis* and all-*trans* forms of *Anabaena* sensory rhodopsin at 77 K. *Biochemistry* 45(14):4362-4370.

25. Eisenhauer K*, et al.* (2012) In channelrhodopsin-2 E90 is crucial for ion selectivity and is deprotonated during the photocycle. *J Biol Chem*.

26. Rothschild KJ, Zagaeski M, & Cantore WA (1981) Conformational changes of bacteriorhodopsin detected by Fourier transform infrared difference spectroscopy. *Biochem. Biophys. Res. Commun.* 103(2):483-489.

27. Engelhard M, Gerwert K, Hess B, Kreutz W, & Siebert F (1985) Light-driven protonation changes of internal aspartic acids of bacteriorhodopsin: an investigation by static and time-resolved infrared difference spectroscopy using [4-^{13}C]aspartic acid labeled purple membrane. *Biochemistry* 24(2):400-407.

28. Braiman MS*, et al.* (1988) Vibrational spectroscopy of bacteriorhodopsin mutants: light-driven proton transport involves protonation changes of aspartic acid residues 85, 96, and 212. *Biochemistry* 27(23):8516-8520.

29. Nie B, Stutzman J, & Xie A (2005) A vibrational spectral maker for probing the hydrogen-bonding status of protonated Asp and Glu residues. *Biophys. J.* 88(4):2833-2847.

30. Takei K, Takahashi R, & Noguchi T (2008) Correlation between the hydrogen-bond structures and the C=O stretching frequencies of carboxylic acids as studied by density functional theory calculations: theoretical basis for interpretation of infrared bands of carboxylic groups in proteins. *J. Phys. Chem. B* 112(21):6725-6731.

31. Kauppinen JK, Moffatt DJ, Mantsch HH, & Cameron DG (1981) Fourier self-deconvolution: a method for resolving intrinsically overlapped bands. *Appl. Spectrosc.* 35:271-276.

32. Barth A (2000) The infrared absorption of amino acid side chains. *Prog. Biophys. Mol. Biol.* 74(3-5):141-173.

33. Sasaki J*, et al.* (1995) Conversion of bacteriorhodopsin into a chloride ion pump. *Science* 269(5220):73-75.

34. Gunaydin LA*, et al.* (2010) Ultrafast optogenetic control. *Nat. Neurosci.* 13(3):387-392.

35. Goormaghtigh E, Cabiaux V, & Ruysschaert JM (1994) Determination of soluble and membrane protein structure by Fourier transform infrared spectroscopy. I. Assignments and model compounds. *Subcell. Biochem.* 23:329-362.

36. Walsh ST*, et al.* (2003) The hydration of amides in helices; a comprehensive picture from molecular dynamics, IR, and NMR. *Protein Sci* 12(3):520-531.

37. Paschek D*, et al.* (2008) The solvent-dependent shift of the amide I band of a fully solvated peptide as a local probe for the solvent composition in the peptide/solvent interface. *Chemphyschem* 9(18):2742-2750.

38. Lórenz-Fonfría VA*, et al.* (2003) Structural and functional implications of the instability of the ADP/ATP transporter purified from mitochondria as revealed by FTIR spectroscopy. *Biophys. J.* 85(1):255-266.

39. Lórenz-Fonfría VA, Kandori H, & Padrós E (2011) Probing specific molecular processes and intermediates by time-resolved Fourier transform infrared spectroscopy: application to the bacteriorhodopsin photocycle. *J. Phys. Chem. B* 115(24):7972-7985.

40. Watanabe HC*, et al.* (2012) Structural model of channelrhodopsin. *J. Biol. Chem.* 287(10):7456-7466.

41. Li H, Robertson AD, & Jensen JH (2005) Very fast empirical prediction and rationalization of protein pK_a values. *Proteins* 61(4):704-721.

42. Heberle J, Oesterhelt D, & Dencher NA (1993) Decoupling of photo- and proton cycle in the Asp85→Glu mutant of bacteriorhodopsin. *Embo J.* 12(10):3721-3727.

43. Iliadis G, Zundel G, & Brzezinski B (1994) Aspartic proteinases — Fourier transform IR studies of the aspartic carboxylic groups in the active site of pepsin. *FEBS Lett.* 352(3):315-317.

44. Otto H*, et al.* (1989) Aspartic acid-96 is the internal proton donor in the reprotonation of the Schiff base of bacteriorhodopsin. *Proc. Natl. Acad. Sci. U. S. A.* 86(23):9228-9232.

45. Perálvarez-Marín A, Márquez M, Bourdelande JL, Querol E, & Padrós E (2004) Thr-90 plays a vital role in the structure and function of bacteriorhodopsin. *J. Biol. Chem.* 279(16):16403-16409.

46. Luecke H, Schobert B, Richter HT, Cartailler JP, & Lanyi JK (1999) Structure of bacteriorhodopsin at 1.55 Å resolution. *J. Mol. Biol.* 291(4):899-911.

47. Nack M*, et al.* (2012) Kinetics of proton release and uptake by channelrhodopsin-2. *FEBS Lett* 586(9):1344-1348.

48. Tombola F, Pathak MM, & Isacoff EY (2006) How does voltage open an ion channel? *Annu. Rev. Cell. Dev. Biol.* 22:23-52.

49. Vogel R*, et al.* (2008) Functional role of the "ionic lock" — An interhelical hydrogen-bond network in family A heptahelical receptors. *J. Mol. Biol.* 380(4):648-655.

50. Sugiyama Y*, et al.* (2009) Photocurrent attenuation by a single polar-to-nonpolar point mutation of channelrhodopsin-2. *Photochem. Photobiol. Sci.* 8(3):328-336.

51. Stehfest K, Ritter E, Berndt A, Bartl F, & Hegemann P (2010) The branched photocycle of the slow-cycling channelrhodopsin-2 mutant C128T. *J. Mol. Biol.* 398(5):690-702.

52. Noguchi T & Sugiura M (2002) Flash-induced FTIR difference spectra of the water oxidizing complex in moderately hydrated photosystem II core films: effect of hydration extent on S-state transitions. *Biochemistry* 41(7):2322-2330.

Figure Legends

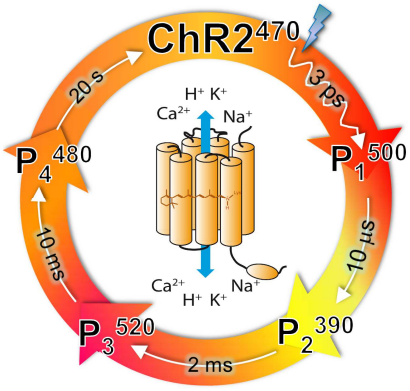

Fig. 1. Scheme of the unidirectional photocycle of ChR2. Superscripts to each reaction intermediate (P_1^{500}, P_2^{390}, P_3^{520}, P_4^{480}) indicate the wavelength of maximum absorption. The photocycle is initiated by the absorption of blue light and each subsequent transition is characterized by the half-life time. Times given correspond to experiments on ChR2 when solubilized in dodecyl-maltoside (25 ^{o}C, neutral pH).

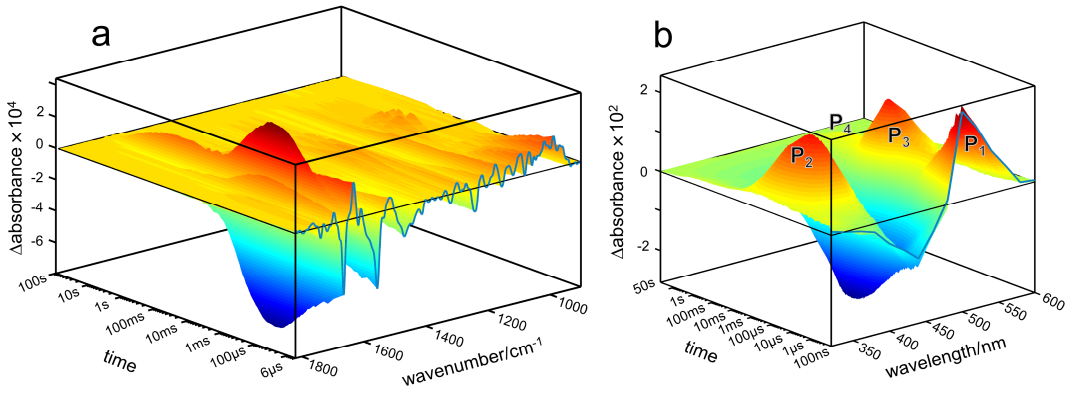

Fig. 2. Time-resolved IR and UV/Vis absorbance changes in ChR2 following retinal photo-isomerization after 10 ns laser excitation. (a) 3D plot of the recorded time-resolved IR and (b) UV/Vis difference spectra.

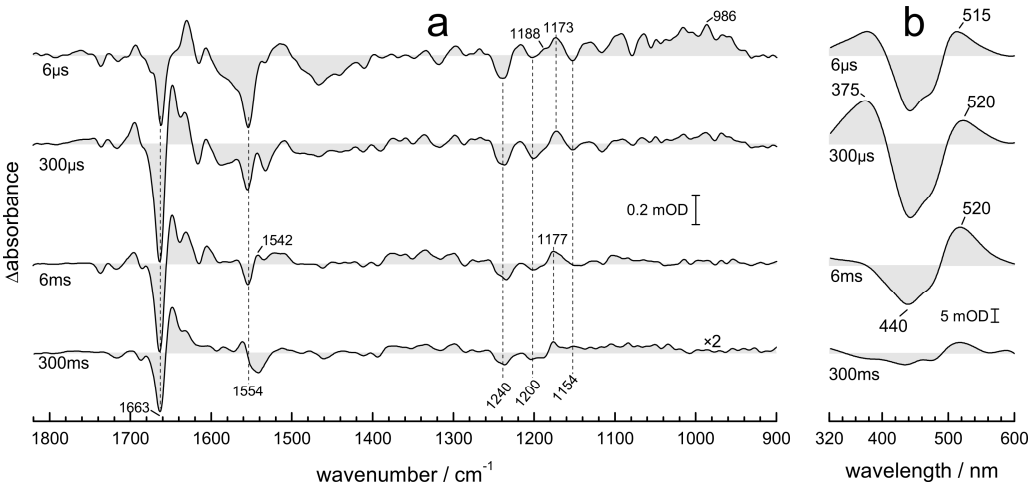

Fig. 3. Time-resolved IR and UV/Vis difference spectra of ChR2 at four selected times after pulsed excitation. (a) Extracted IR difference spectra. (b) Extracted UV/Vis difference spectra showing from the positive bands that the extracted spectra correspond mainly to the P_1^{500} (6 µs), P_2^{390} (300 µs), P_3^{520} (6 ms) and P_4^{480} (300 ms) intermediates, respectively. The positive contribution from P_1^{500} appears up-shifted to 515 nm as a result of the spectral overlap by the absorption of the initial dark state (14).

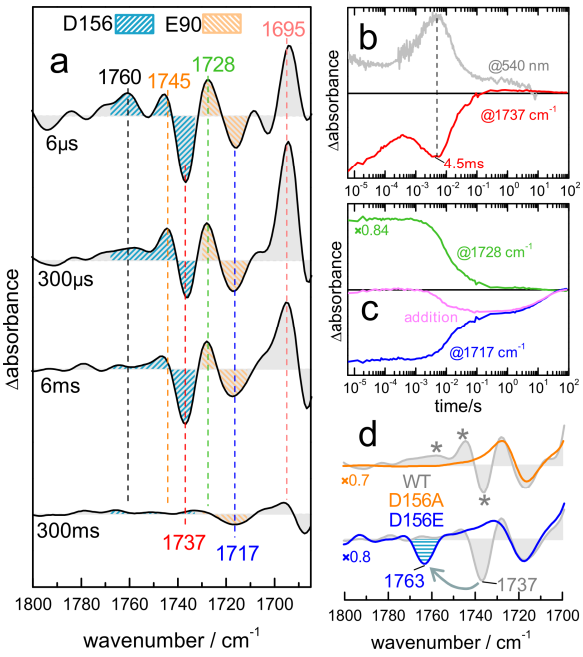

Fig. 4. Identification of the Schiff base proton donor group. (a) IR difference spectra in the carboxylic region of wild-type ChR2 after FSD. Bands assigned either to the C=O stretching vibration of protonated D156 or E90, are indicated by hatched areas. (b) Kinetics of the negative band at 1737 cm^{-1} (red trace) compared to the kinetics at 540 nm (gray trace) measured on the same sample. The kinetics at 540 nm reflects the rise and decay of the P_3^{520} state. (c) Kinetics of the negative band at 1717 cm^{-1} (blue trace) and the positive band at 1728 cm^{-1} (green). The addition of both traces (magenta) resolves protonation changes of E90. (d) Top: difference spectra of the P_2^{390} state of wild-type ChR2 (gray trace) and the D156A mutant (orange) extracted at 300 µs and at 6 ms after the flash, respectively. Bottom: difference spectra of the P_3^{520} state of wild-type ChR2 (gray trace) and the D156E mutant (blue) extracted at 6 ms after the flash. Missing and shifted bands are indicated by asterisks and arrows, respectively.

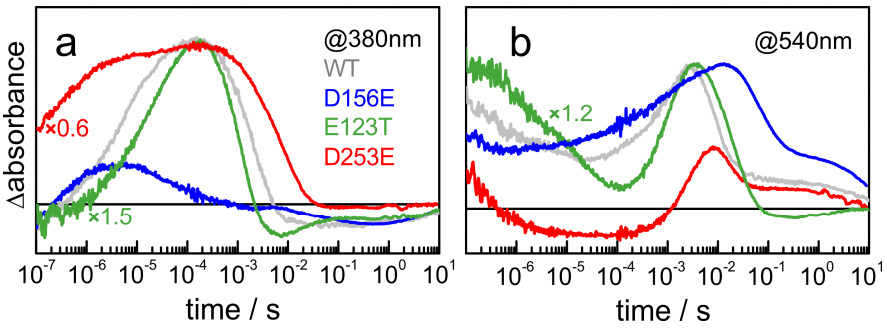

Fig. 5. Transient absorbance changes in the UV/Vis range after pulsed excitation of wild-type ChR2 (grey trace) and variants D156E (blue), E123T (green) and D253E (red). (a) The blue-shifted intermediate P_2^{390} was probed at 380 nm and (b) the red-shifted early P_1^{500} and the late P_3^{520} intermediates were probed at 540 nm. Some of the transients have been scaled in amplitude to facilitate the comparison.

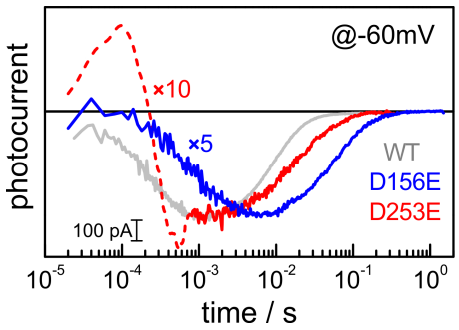

Fig. 6. Time-resolved photocurrents of ChR2 after pulsed laser excitation. Wild-type ChR2 (gray trace), and variants D156E (blue) and D253E (red) have been expressed in HEK293 cells and the whole cell patch-clamp technique has been applied. The currents were recorded at room temperature (~22 ^{o}C) at a holding potential of -60 mV. The traces were normalized to the maximum current amplitude of wild-type ChR2 to facilitate kinetic comparison. The accelerated kinetics of channel opening in the D253E mutant could not be resolved due to the response time of the electrical recordings in this experiment (red dashed trace, τ_{RC}~50-100 µs, see **Supplementary Information** for further details).

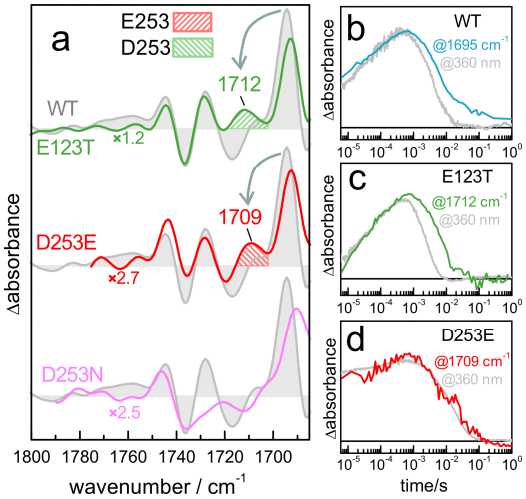

Fig. 7. Identification of the acceptor of the Schiff base proton. (a) IR difference spectra in the carboxylic region of the P_2^{390} state of E123T (green), D253E (red) and D253N variants (magenta). Spectra have been normalized to the wild type (grey) using the retinal fingerprint region. Band shifts are indicated by arrows and the vibrational assignment by hatched areas. (b) Kinetic trace at 1696 cm^{-1} (light blue trace) in comparison to the rise and decay of the P_2^{390} state (measured at 360 nm) for wild-type ChR2. (c) Kinetics at 1713 cm^{-1} (green trace) and of the P_2^{390} state (gray trace) of the E123T variant . (d) Kinetics at 1710 cm^{-1} (red trace) and of the P_2^{390} state (gray trace) of the D253E variant. The intensity of the IR traces were scaled to match the intensity of the respective traces at 360 nm.

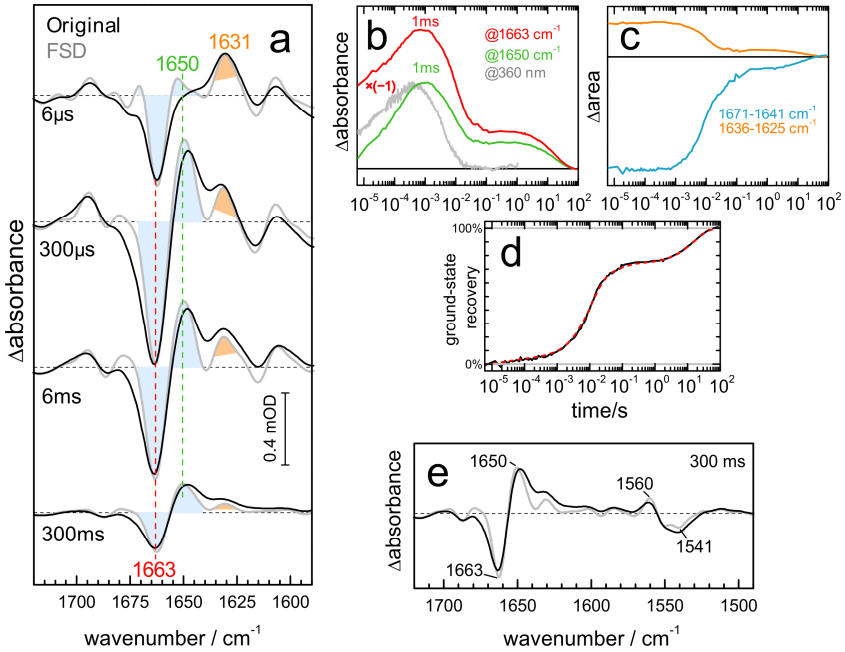

Fig. 8. Changes in amide I and II vibrations of the protein backbone during the ChR2 photocycle. (a) IR differences in the raw spectra (black lines) and after applying FSD (gray lines). Relevant bands are indicated, as well as their integrated areas. (b) Kinetics of the intensity changes at 1663 cm^{-1} (red trace) and 1650 cm^{-1} (green trace). Scaled kinetics of P_2^{390} measured at 360 nm on the same sample used for the IR experiments (gray trace). (c) Kinetics of the negative band at 1663 cm^{-1} probed by integrating the area from 1671 to 1641 cm^{-1} (light blue trace). This procedure canceled the overlapping contribution from the hydration of helices by assuming similar amide I extinction coefficients for non-hydrated and hydrated amide groups. The kinetics of the positive band at 1631 cm^{-1} was determined by tracing the integrated area between 1636 and 1625 cm^{-1} (orange trace). (d) Kinetics of the band area integrated between 1249 and 1227 cm^{-1} which reflects ground-state recovery (black trace), and an exponential fit (dashed red trace). (e) IR difference spectrum of P_4^{480}, including the amide I and II region (black line). The FSD-treated spectrum is also shown (gray line). Bands assigned to the hydration of α-helices are labeled.

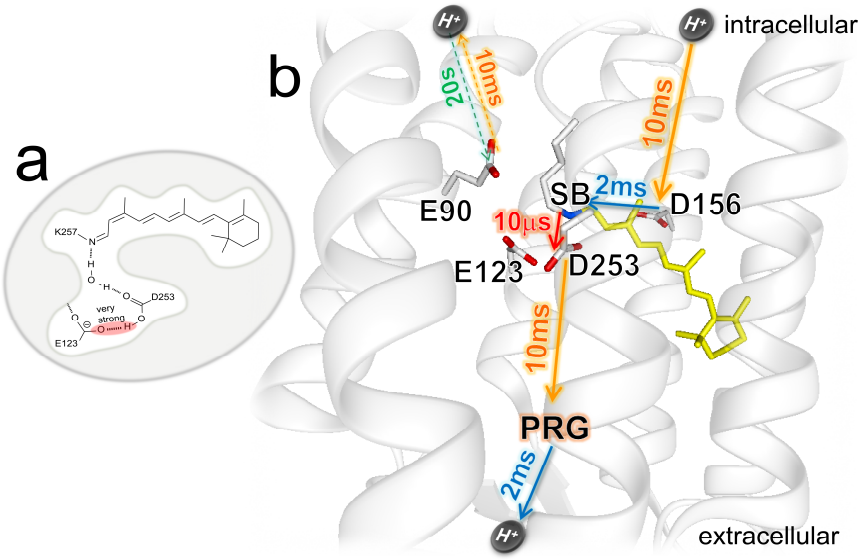

Fig. 9. Proton transfers in the ChR2 photocycle. (a) Schematic representation of the proposed direct H-bonding of D253 with E123 in the P_2^{390} state. Other H-bonds are purely tentative. (b) Cartoon of ChR2 based on the C1-C2 structure (6), showing relevant carboxylic groups and the proposed proton transfers reactions along with their half-life times. Proton release and uptake from E90 is arbitrary set to the intracellular side. The location of the proton release group (PRG) is unknown but tentatively placed in the extracellular domain of ChR2.